Stem Cell Reports
Article
ISSCR
OPEN ACCESS

Morphological and Molecular Defects in Human Three-Dimensional Retinal Organoid Model of X-Linked Juvenile Retinoschisis

Kang-Chieh Huang,[1,2,3] Mong-Lien Wang,[1,2,4,5] Shih-Jen Chen,[4,6] Jean-Cheng Kuo,[7,8] Won-Jing Wang,[7] Phan Nguyen Nhi Nguyen,[1,2] Karl J. Wahlin,[9] Jyh-Feng Lu,[10] Audrey A. Tran,[11] Michael Shi,[11] Yueh Chien,[1] Aliaksandr A. Yarmishyn,[1] Ping-Hsing Tsai,[1,2] Tien-Chun Yang,[1,2] Wann-Neng Jane,[12] Chia-Ching Chang,[13] Chi-Hsien Peng,[14] Thorsten M. Schlaeger,[11,*] and Shih-Hwa Chiou[1,2,4,6,15,*]

[1]Department of Medical Research, Taipei Veterans General Hospital, Taipei 11217, Taiwan
[2]Institute of Pharmacology, National Yang-Ming University, Taipei 11221, Taiwan
[3]Department of Biology, Indiana University-Purdue University Indianapolis, Indianapolis, IN 46202, USA
[4]School of Medicine, National Yang-Ming University, Taipei 11221, Taiwan
[5]Institute of Food Safety and Health Risk Assessment, National Yang-Ming University, Taipei 11221, Taiwan
[6]Department of Ophthalmology, Taipei Veterans General Hospital, Taipei 11217, Taiwan
[7]Institute of Biochemistry and Molecular Biology, National Yang-Ming University, Taipei 11221, Taiwan
[8]Cancer Progression Research Center, National Yang-Ming University, Taipei 11221, Taiwan
[9]Shiley Eye Institute, University of California San Diego, La Jolla, CA 92093, USA
[10]School of Medicine, Fu-Jen Catholic University, New Taipei City 24205, Taiwan
[11]Stem Cell Program and Division of Hematology/Oncology, Boston Children's Hospital and Dana-Farber Cancer Institute, Harvard Stem Cell Institute, Harvard Medical School, Boston, MA 02115, USA
[12]Institute of Plant and Microbial Biology, Academia Sinica, Taipei 11529, Taiwan
[13]Department of Biological Science and Technology, National Chiao Tung University, Hsinchu 300, Taiwan
[14]Department of Ophthalmology, Shin Kong Wu Ho-Su Memorial Hospital & Fu-Jen Catholic University, Taipei 11101, Taiwan
[15]Genomic Research Center, Academia Sinica, Taipei 11529, Taiwan
*Correspondence: thorsten.schlaeger@childrens.harvard.edu (T.M.S.), shchiou@vghtpe.gov.tw (S.-H.C.)
https://doi.org/10.1016/j.stemcr.2019.09.010

SUMMARY

X-linked juvenile retinoschisis (XLRS), linked to mutations in the *RS1* gene, is a degenerative retinopathy with a retinal splitting phenotype. We generated human induced pluripotent stem cells (hiPSCs) from patients to study XLRS in a 3D retinal organoid *in vitro* differentiation system. This model recapitulates key features of XLRS including retinal splitting, defective retinoschisin production, outer-segment defects, abnormal paxillin turnover, and impaired ER-Golgi transportation. *RS1* mutation also affects the development of photoreceptor sensory cilia and results in altered expression of other retinopathy-associated genes. CRISPR/Cas9 correction of the disease-associated C625T mutation normalizes the splitting phenotype, outer-segment defects, paxillin dynamics, ciliary marker expression, and transcriptome profiles. Likewise, mutating *RS1* in control hiPSCs produces the disease-associated phenotypes. Finally, we show that the C625T mutation can be repaired precisely and efficiently using a base-editing approach. Taken together, our data establish 3D organoids as a valid disease model.

INTRODUCTION

X-linked juvenile retinoschisis (XLRS), named after the distinctive retinal splitting phenotype, is a relatively common early-onset degenerative disease of the central retina with a worldwide prevalence at 1/5,000 to 1/20,000 (George et al., 1995; Molday et al., 2012). Clinical features of XLRS include mild to severe and progressive loss of central vision, radial streaks arising from foveal schisis, splitting of inner retinal layers in the peripheral retina, retinal detachment, and vitreous hemorrhage (Tantri et al., 2004). *RS1*, the gene implicated in XLRS, encodes a highly conserved secreted extracellular protein called retinoschisin (RS1) (Sauer et al., 1997). *RS1* is composed of an N-terminal signal sequence that mediates protein secretion via the ER pathway (Sauer et al., 1997; Wu and Molday, 2003), followed by *RS1* and discoidin domains and a C-terminal segment specifically expressed in the retina and pineal gland (Takada et al., 2006). More than 190 mutations of *RS1* gene have been associated with XLRS, and most of them are located within the discoidin domain, causing protein misfolding and retention in the ER (Molday et al., 2012; Wang et al., 2002; Wu and Molday, 2003).

RS1 protein is mainly localized at the extracellular surfaces of the inner segments of rod and cone photoreceptors in the retina as well as in bipolar cells and two plexiform layers (Molday et al., 2001). Furthermore, an *Rs1* knockout mouse study revealed that *Rs1* is essential for maintaining cell-to-cell interactions of retinal cells (Reid et al., 2003). Although mouse models can be a useful tool for studying the disease mechanism of retinopathies, mouse and human retinas are not equivalent. For example, the rod-to-cone ratios differ significantly between mouse (a nocturnal species) and human foveas (Mustafi et al., 2009; Peirson et al., 2018; Volland et al.,

2015). Besides, several mouse models of retinal disorders have failed to recapitulate disease-relevant phenotypes (Garanto et al., 2013; Liu et al., 1997). This leaves questions as to whether mouse *in vivo* models are a suitable surrogate for studying the functions of normal and mutant human *RS1* in retinal development or XLRS. Similarly, immortalized human photoreceptor cell models are lacking, making it difficult to uncover the interactions between *RS1* and other factors involved in photoreceptor function and biogenesis.

Human induced pluripotent stem cells (hiPSCs) have emerged as a promising alternative to animal-based disease modeling systems. hiPSCs can be generated from patients, expanded indefinitely, and differentiated into specific cells and tissue types relevant for disease modeling (Chou et al., 2017; Meyer et al., 2011; Parfitt et al., 2016; Singh et al., 2013). Moreover, hiPSCs allow the discovery and functional validation of genotype-phenotype relationships in patient-specific genetic backgrounds. Several recent studies have utilized hiPSCs to study human hereditary retinopathies (Deng et al., 2018; Ohlemacher et al., 2016; Parfitt et al., 2016). However, so far, hiPSC-derived retinal cells have not been used to study the molecular and cellular mechanisms that underlie the pathology of XLRS. In this study, we enrolled XLRS patients with *RS1* mutations for generating patient-specific hiPSCs, and further established 3D retinal organoids from the patient-specific hiPSCs for disease modeling of XLRS. We show that XLRS-patient-specific hiPSC-derived retinal organoids exhibit structural defects similar to those found in patient retinas. Phenotypes include a reduction in rod and cone cell frequencies, defects in the connecting cilium, and accelerated paxillin dynamics, as well as a progressive loss of expression of *IQCB1* and *OPA1*, two retinal genes associated with hereditary ocular diseases. Importantly, the observed phenotypes were abrogated in retinal organoids generated from gene-repaired hiPSCs, validating this system as a tool to study XLRS. Furthermore, we generated multiple sets of isogenic hiPSCs to confirm specificity of the genotype-phenotype relationships. CRISPR repair was efficient (50%), but also generated frequent indels. To avoid generating inadvertent indels, we evaluated Cas9-ABE7.10 mediated base editing as an alternative method to repair the *RS1* locus and found it to be equally efficient.

RESULTS

Generation of the XLRS-Patient-Specific hiPSC-Derived 3D Retinal Organoids as an *In Vitro* Retinoschisis Disease Model

Two patients diagnosed with XLRS (Pt-1 and Pt-2) and two control donors (Ctrl-1 and Ctrl-2) were enrolled in this study. Two XLRS patients exhibited abnormal retinal splitting and bilateral macular atrophy with cartwheel appearance, as detected by dilated indirect ophthalmoscopy (Figure 1A). Full-field electroretinography (ERG) revealed markedly reduced amplitude in dark-adapted 0.01 ERG (rod response), light-adapted 3.0 ERG (cone response), and light-adapted 3.0 flicker responses (Figure S1A). Pt-1 and Pt-2 were found to carry *RS1* mutations respectively at c.625C>T (p.R209C) and c.488G>A (p.W163X) (Figure S1B). Peripheral blood mononuclear cells from XLRS patients and control donors were reprogrammed into hiPSCs using the non-viral episomal plasmid protocol (Okita et al., 2013) (Table S1). At least two independent hiPSC clonal lines were generated from each XLRS patient or control donor, and all control-donor- and patient-derived hiPSC clones exhibited normal karyotypes and expressed human PSC markers (Figures S2A–S2C). Genotyping of the XLRS patient-derived hiPSC clones confirmed the presence of the respective *RS1* mutations at c.625C>T and c.488G>A (Figure 1B) (Peng et al., 2018). We then applied a stepwise three-dimensional (3D) retinal organoid formation protocol (Figure 1C) (Ohlemacher et al., 2015; Zhong et al., 2014) on the hiPSCs of control donors (Ctrl-1 and Ctrl-2) and XLRS patients (Pt-1 and Pt-2) to generate 3D retinal organoids. In the early stage of retinal differentiation, control and patient-derived organoids expressed markers of anterior neuroectoderm commitment (LHX2, PAX6, and OTX2) at day 13 (Figure S3A). On day 20, the densely packed neural rosettes were isolated and cultured in suspension, which resulted in formation of 3D retinal cups (RCs) by day 30 (Figure 1D). At this stage, RCs contained numerous VSX2- and Ki-67-positive retinal progenitor cells (Figure S3B). We continued the differentiation of control RCs (Ctrl-1 and Ctrl-2) and patient RCs (Pt-1 and Pt-2) to day 150. The expression of the photoreceptor-specific protein RCVRN (Recoverin) increased continuously from day 90 to day 150 (Figure 1E). In contrast, while RS1 expression increased over time in control RCs, its overall expression was reduced in Pt-1 RCs and virtually absent in Pt-2 RCs (Figure 1E). Moreover, we also observed an overt retinoschisis phenotype in RCs derived from both patients from day 100, but not in control RCs, during differentiation (Figure 1F), which is reminiscent of the clinical characteristics of XLRS, i.e., the splitting (schisis) of the retina between outer and inner nuclear layers. In addition, immunofluorescent staining of RS1 protein in patient RCs confirms the location of RS1 proteins in the outer layer of the developing retina and the significantly decreased expression from day 120 in comparison with control RCs (Figure 1G).

To further validate the incidence of retinoschisis and the size of schisis area in *RS1*-mutant iPSC RCs, we compared patient RCs with control RCs at 150 days. We first measured

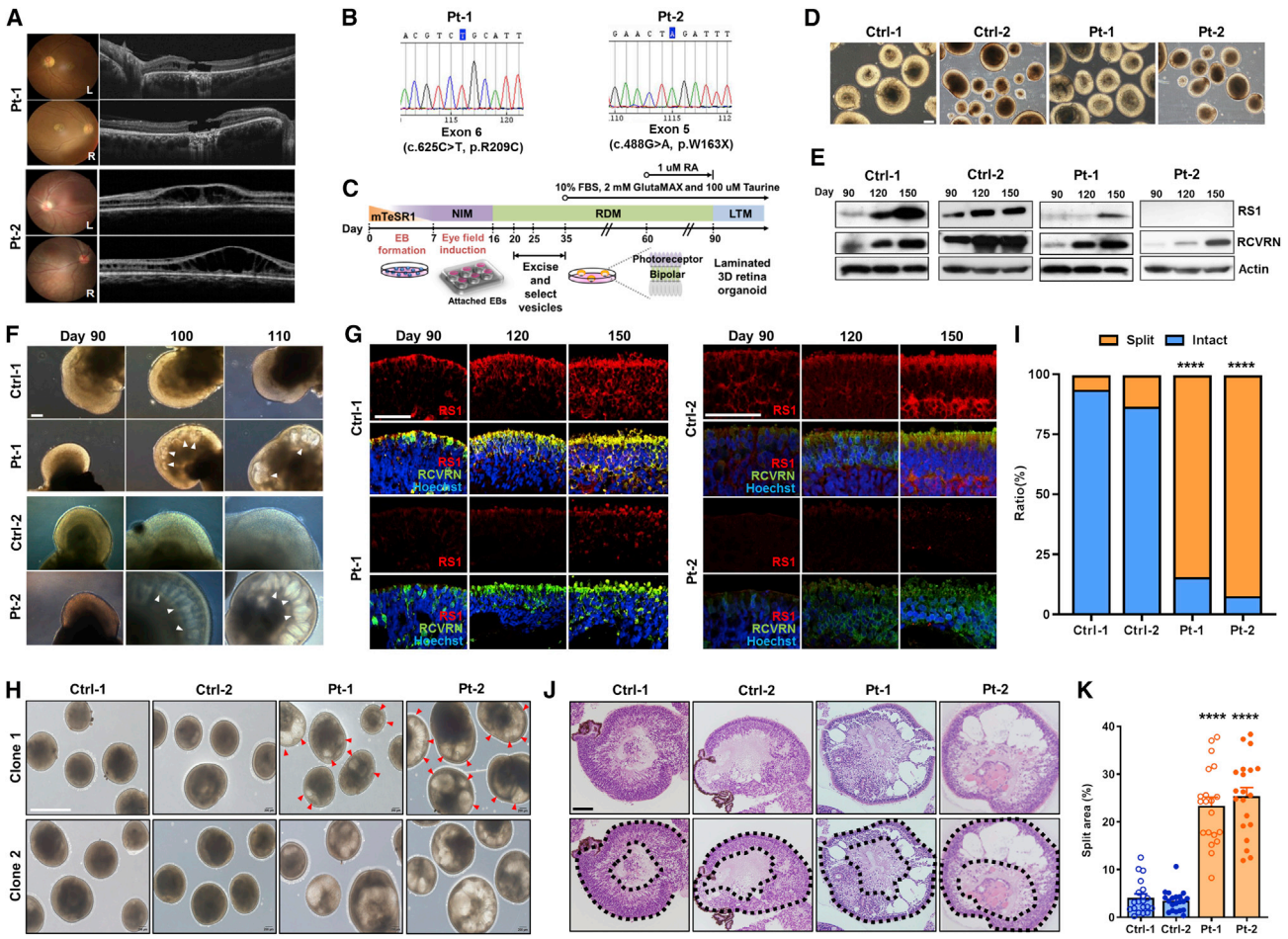

Figure 1. 3D Retinal Organoids Modeling XLRS from Patient-Specific hiPSCs

(A and B) Color fundus photograph (left panel) and optical coherence tomography (OCT) images (right panel) of two X-linked juvenile retinoschisis (XLRS) patients (Pt-1 and Pt-2). (B) DNA sequencing of *RS1* mutation in hiPSCs (B). The position of a nucleotide change 625C>T (Pt-1) and 488G>A (Pt-2).

(C) Schematic diagram of differentiation procedure from iPSCs into 3D retinal organoids.

(D) Morphology of 3D retinal cups (RCs) at day 30 of differentiation in two controls (Ctrl-1 and Ctrl-2), Pt-1, and Pt-2 lines. Scale bar, 200 μm.

(E) Western blotting of RCVRN and RS1 expression at distinct differentiated time points of Ctrl-1, Ctrl-2, Pt-1, and Pt-2 RCs.

(F) Bright-field images of control RCs and patient RCs at days 90, 100, and 110 of differentiation. The white arrows indicate the splitting (schisis) regions within patient RCs. Scale bar, 200 μm.

(G) Immunofluorescence staining of RS1 (red) and photoreceptor marker RCVRN (green) in the outer layer of RCs at days 90, 120, and 150. Scale bar, 50 μm.

(H) Bright-field images from each of the two clones of control RCs and patient RCs at day 150 of differentiation. The red arrowheads indicate the splitting (schisis) regions within patient RCs. Scale bar, 1,000 μm.

(I) Quantification of the ratio of RCs between schisis and non-schisis phenotype. For each sample, a total of over 80 RCs from two iPSC clones were counted, and the data presents the mean value from three independent experiments. Chi-squared test was used for statistical analysis with $p < 0.0001$.

(J) H&E-stained 150-day RCs. The lower panel shows the retinal nuclear layer in RCs and the areas (between the two dotted lines) that were used for splitting layer quantification. The percentage of splitting layer was calculated by the ratio of the white (cell-free) area and the total area between outer nuclear layer and inner nuclear layer of each RC. Scale bar, 200 μm.

(K) Quantification of splitting layer area in 150-day control RCs and patient RCs (n = 20 for each group from 3 independent experiments). Error bars represent SEM. One-way ANOVA was used for statistical analysis (****$p < 0.0001$). See also Figures S1–S4.

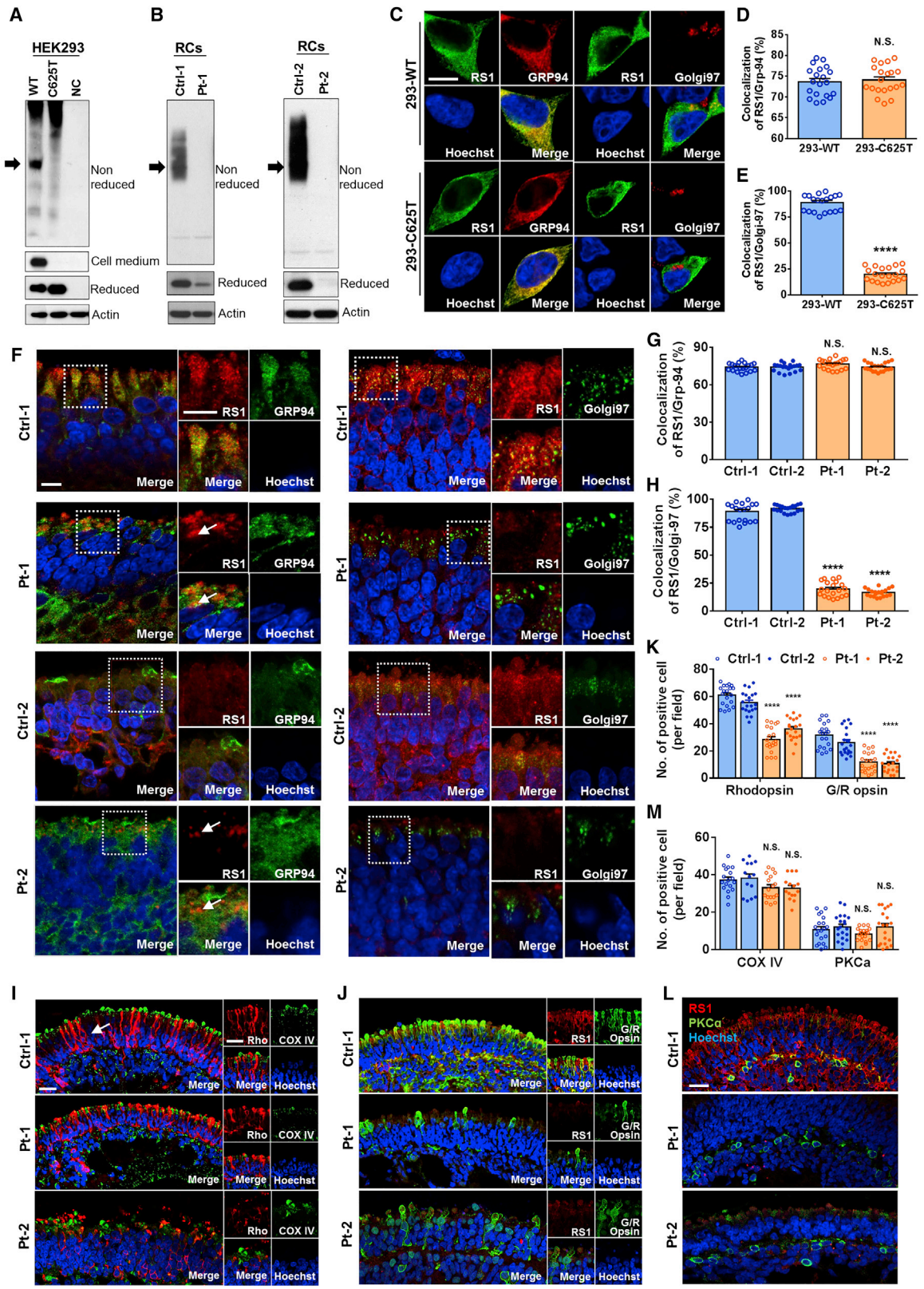

(legend on next page)

the penetration of the schisis phenotype in the RCs harboring *RS1* mutation. We evaluated about 200 RCs (about 25 per hiPSC-clone-derived RCs) from two independent hiPSC clones for each of the two patients and for each of the two healthy donor controls. All sets of mutant RCs showed at least 80% of abnormal-looking RCs with cyst/schisis-like features while fewer than 20% of healthy-donor-derived RCs had that phenotype. All pairwise comparisons of mutant and normal donor RC datasets reached the level of statistical significance (Figures 1H–1I and S4A). As a measure of the magnitude of the defect we calculated the size of the split area between the outer nuclear layer (ONL) and inner nuclear layer (INL) of 150-day control and patient RCs (Figure S3C). The average size of the split area was increased in cross-sections of patient-derived mutant RCs compared with control RCs (Figures 1J, 1K, and S4B). These data indicated that RS1 protein expression positively correlates with the integrity of RC structure, especially the attachment between ONL and INL, and reflected the hiPSC-derived 3D retinal organoids as a suitable *in vitro* retinoschisis disease model.

Mutated *RS1* Leads to Defects on RS1 Protein Secretion and Neuroretinal Outer-Segment Development

RS1 is a secreted protein that forms a disulfide-linked homo-octameric complex (Molday et al., 2012). To examine whether *RS1* mutation affects its homo-octameric complex formation, we separated the lysates from wild-type and C625T-mutant *RS1*-transfected HEK293 cells on a non-reducing gel, and showed that wild-type RS1 migrated to a size of about 180 kDa, consistent with the expected size of RS1 octamers (Figure 2A). In contrast, C625T-mutant *RS1*, despite robust expression of the monomer, failed to produce the mature complex and failed to secrete into the culture medium (Figure 2A). Day-120 RCs derived from patients 1 and 2 similarly failed to produce mature RS1 octamers, and total RS1 protein expression was much reduced in Pt-1 RCs or virtually absent in Pt-2 RCs (Figure 2B). Prior to secretion, RS1 needs to transit through and mature in the ER and the Golgi apparatus (Wang et al., 2002; Wu and Molday, 2003). To examine where the process fails with mutant RS1, we co-immunostained the cells for RS1 and the ER marker GRP94 or the Golgi marker Golgi97 in RS1-overexpressing HEK293 cells and day-150 RCs. In the HEK293 cells, wild-type RS1 clearly co-localized with both GRP94 and Golgi97 while C625T mutant RS1 only co-localized efficiently with GRP94 and showed little overlap with Golgi97 (Figures 2C–2E). Similarly, in the 150-day patient-derived RCs, RS1 co-localization with GRP94 was reduced but remained readily detectable, while virtually no mutant protein co-localized with the Golgi marker (Figures 2F–2H). Our results confirm the RS1 secretion defect that may result from incomplete processing and transport of the protein.

We further investigated the developing photoreceptor and bipolar layers, where RS1 is known to be expressed (Molday et al., 2001), of the retinal structures of control and patient hiPSC-derived RCs. RCs derived from both patients contained significantly fewer photoreceptor cells, as assessed by rhodopsin and G/R opsin immunofluorescence microscopy (Figures 2I and 2J). Cone cell (G/R opsin) numbers were more severely reduced than rod cell (rhodopsin) numbers (Figure 2K). In contrast, the frequency of inner-segment (COX IV) and bipolar (PKCα) cells was not disturbed in patient-derived RCs (Figures 2I, 2L, and 2M), despite the continued severe reduction in RS1 expression (Figures 2J–2L). These results demonstrated a correlation between mutated RS1 and the outer-layer defects, which leads to the defect of protein

Figure 2. Schisis Phenotype and Defective Photoreceptor Formation in *RS1*-Mutated 3D RCs

(A) Western blotting of RS1 protein expression in transfected wild-type and C625T-mutated HEK293 cells under reducing and non-reducing gel conditions.

(B) Western blotting of Ctrl-1, Pt-1, Ctrl-2, and Pt-2 RCs at 120 days. The arrow indicates RS1 that migrated as ~180-kDa complex in non-reducing condition. Actin was used as internal control.

(C) Immunofluorescence staining of RS1 with ER (GRP94) and Golgi (Golgi97) 48 h after transfection of HEK293 cells. Scale bar, 10 μm.

(D and E) Quantification of RS1 co-localization with GRP94 (D) and Golgi97 (E) (n = 20 images from 3 independent experiments).

(F) Immunofluorescence staining of RS1 with GRP94 and Golgi97 in 150-day control and C625T RCs. The right panel is a higher-magnification image of the left panel marked with a dotted box. The arrows indicate the prominent mutant RS1-positive signal in C625T-RCs. Scale bar, 10 μm.

(G and H) Quantification of RS1 co-localization with GRP94 (G) and Golgi97 (H) (n = 20 images from 3 independent experiments).

(I–M) Immunofluorescence staining of rhodopsin, COX VI (labeled inner segment) (I), G/R opsin, RS1 (J), and PKCα (L) in 150-day control RCs and C625T-RCs. (I) The arrows indicate the normal rod cell morphology in control RCs. Scale bar, 20 μm. (K) Quantification of cell density of rhodopsin and G/R opsin in 150-day control and C625T-RCs (n = 20 images from 3 independent experiments). (M) Quantification of cell density of COX IV and PKCα in 150-day control and C625T-RCs (n = 20 images from 3 independent experiments).

Error bars represent SEM. Unpaired Student's t test (D and E) and one-way ANOVA were used for statistical analysis (****$p < 0.0001$; N.S., not significant).

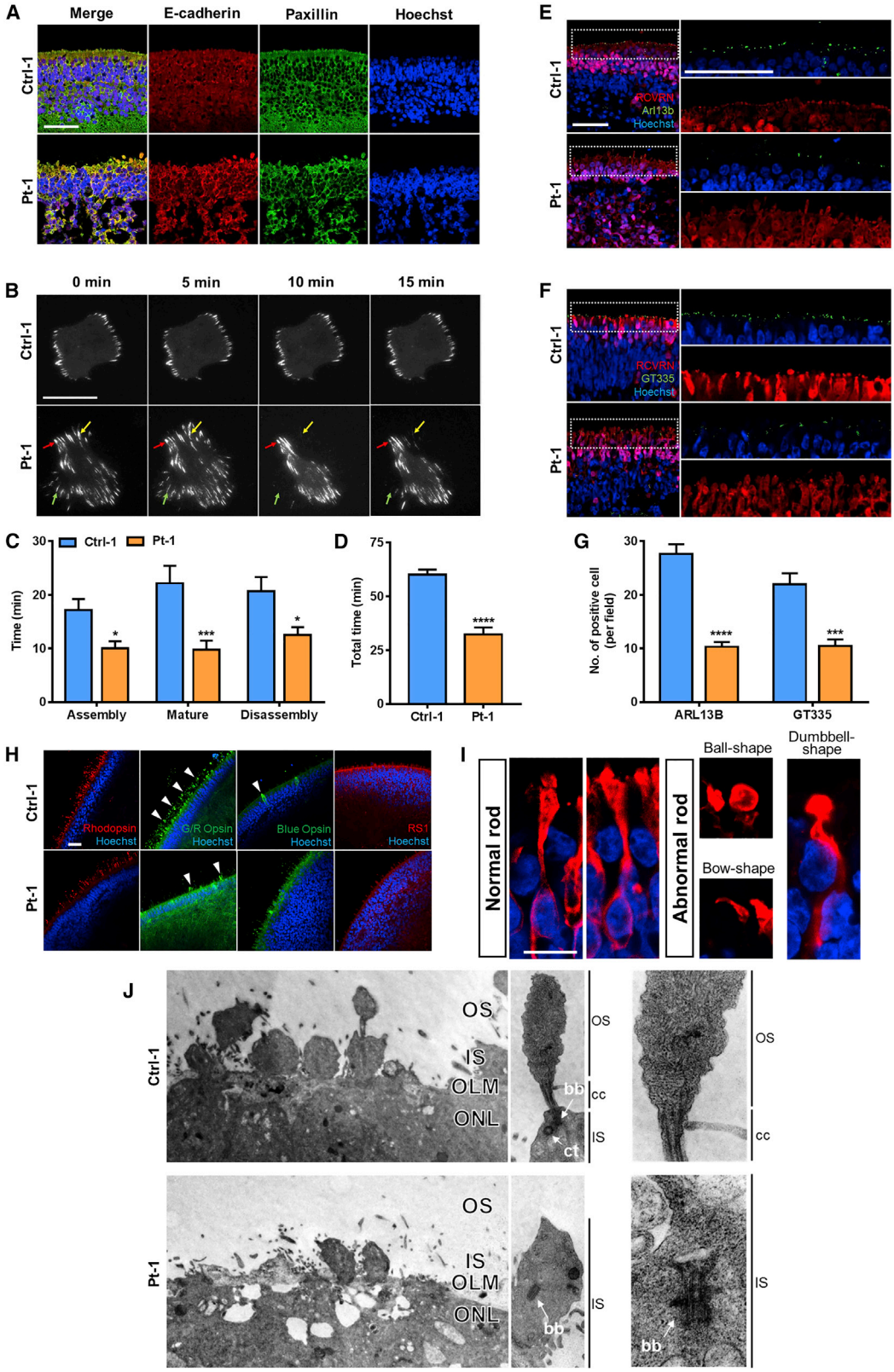

(legend on next page)

secretion process and photoreceptor development cells in 3D organoids.

Mutated *RS1* Disturbs the Neuronal Adhesion Capabilities and the Outer-Segment Maturation

E-Cadherin is a homotypic cell-cell adhesion mediator expressed in the neural retina (Xu et al., 2002), and RS1's interaction with the Na/K-ATPase transmembrane signalosome complex on photoreceptor and bipolar cells (Molday et al., 2007) provides a possible link via SRC and FAK to Paxillin, a focal adhesion protein critical for cell-matrix interactions (Liang et al., 2006; Plossl et al., 2017; Richardson et al., 1997; Zaidel-Bar et al., 2007). To reveal potential adhesion defects, we therefore stained 150-day RCs for E-cadherin and paxillin. While the expression levels and distribution of these proteins were seemingly unaffected, the retinal tissue nevertheless appeared much less well organized in patient-derived RCs, with many large intercellular gaps (Figure 3A). When we measured the assembly and disassembly times of paxillin in dissociated retina cells, in cells from dissociated 150-day RCs (Figure 3B) we observed accelerated dynamics (Figures 3B and 3C), resulting in a faster focal adhesion turnover in patient-derived cells (Figure 3D; Videos S1 and S2). The faster cycling of paxillin thus may contribute to the observed structural defects and diminished phototransduction in XLRS.

The connecting cilium is a structure critical for photoreceptor cell maturation and intraflagellar transport between the inner segment and the light-sensing outer segment (Adams et al., 2007; De Robertis, 1956). The defect of outer-segment development prompted us to investigate the structure of connecting cilia in *RS1* mutated RCs. We stained for the cilia markers ARL13B and glutamylated tubulin (GT335) in 150-day RCVRN-positive RCs. ARL13B and GT335 signals were both significantly reduced in patient-derived RC as compared with control RCs (Figures 3E–3G), implying that *RS1*-mutant photoreceptor cells contained defective connecting cilia and outer-segment structures.

Long-term differentiation triggered outer-segment formation after day 180, and by day 210 control RCs contained numerous mature-looking rod and cone cells and a distinctive outer-segment layer. However, in patient-derived RCs, rod cells (rhodopsin) continued to be less abundant, and very few G/R opsin and virtually no proper blue-opsin cone cells were present (Figure 3H), in line with the reduced frequency and immature appearance or abnormal shape of neuroretinal outer segment and photoreceptor cells observed in patient-derived RC at earlier time points. Moreover, by immunofluorescent staining and imaging of 150-day optic vesicles we found that patient-derived RC rod cells were frequently deformed (Figure 3I). To examine the organization of photoreceptors in more detail, we used transmission electron microscopy (TEM). Control RC photoreceptors at 210 days showed properly formed features including the ONL, outer limiting membrane, and inner-segment and outer-segment layers (Figure 3J). Higher-magnification images revealed the centriole, basal body, and transition zone of the connecting cilium between the inner and outer segment of control RCs (Figure 3J). In contrast, patient-derived RC (Pt-1, c.625C>T) photoreceptors frequently lacked a distinct outer segment and contained large vesicles as well as basal bodies that were localized in the center rather than at the apical surface of the inner segment (Figure 3J). In conclusion, these data revealed the abnormal morphology and immature appearance of the outer segment, reduced numbers of rod and cone cells, and faster focal adhesion turnover in patient-derived RCs.

Figure 3. Disorganized Cilia Formation and Loss of Adhesion in XLRS Retinal Organoids

(A) Immunofluorescence staining of E-cadherin and paxillin in 150-day RCs. Scale bar, 50 μm.

(B) TIRFM images showing focal adhesion dynamics in transfected mApple-paxillin photoreceptor cells. The arrows indicate the paxillin dynamics over time in C625T mutant photoreceptor cells. Scale bar, 40 μm.

(C and D) Quantification of focal adhesion dynamics by measuring assembly, mature state, disassembly (C), and total duration (D) time lapse of mApple-paxillin expression (n = 14 control RCs and 10 C625T-RCs from 3 independent experiments).

(E and F) Immunofluorescence staining of ARL13B (E) and tubulin GT335 (F) in 150-day RCs. A higher-magnification image in the right panel is the left panel marked with a dotted box. Scale bar, 50 μm.

(G) Quantification of cilium density of immunofluorescence in 150-day RCs from higher-magnification images. (n = 4 images from 3 independent experiments).

(H) Immunofluorescence staining of rhodopsin, G/R opsin, blue opsin, and RS1 in 210-day whole-mount RCs. The arrows indicate the positive G/R and blue-opsin signal within outer-segment layer. Scale bar, 50 μm.

(I) Classified shape of rod cell by rhodopsin staining. Scale bar, 10 μm.

(J) Transmission electron micrographs of 210-day RCs. OS, outer segment; IS, inner segment; OLM, outer limiting membrane; ONL, outer nuclear layer; cc, connecting cilium; bb, basal body; ct, centriole. Scale bar, 0.5 μm.

Error bars represent SEM. Unpaired Student's t test was used for statistical analysis (*$p < 0.05$; ***$p < 0.001$; ****$p < 0.0001$). See also Videos S1 and S2.

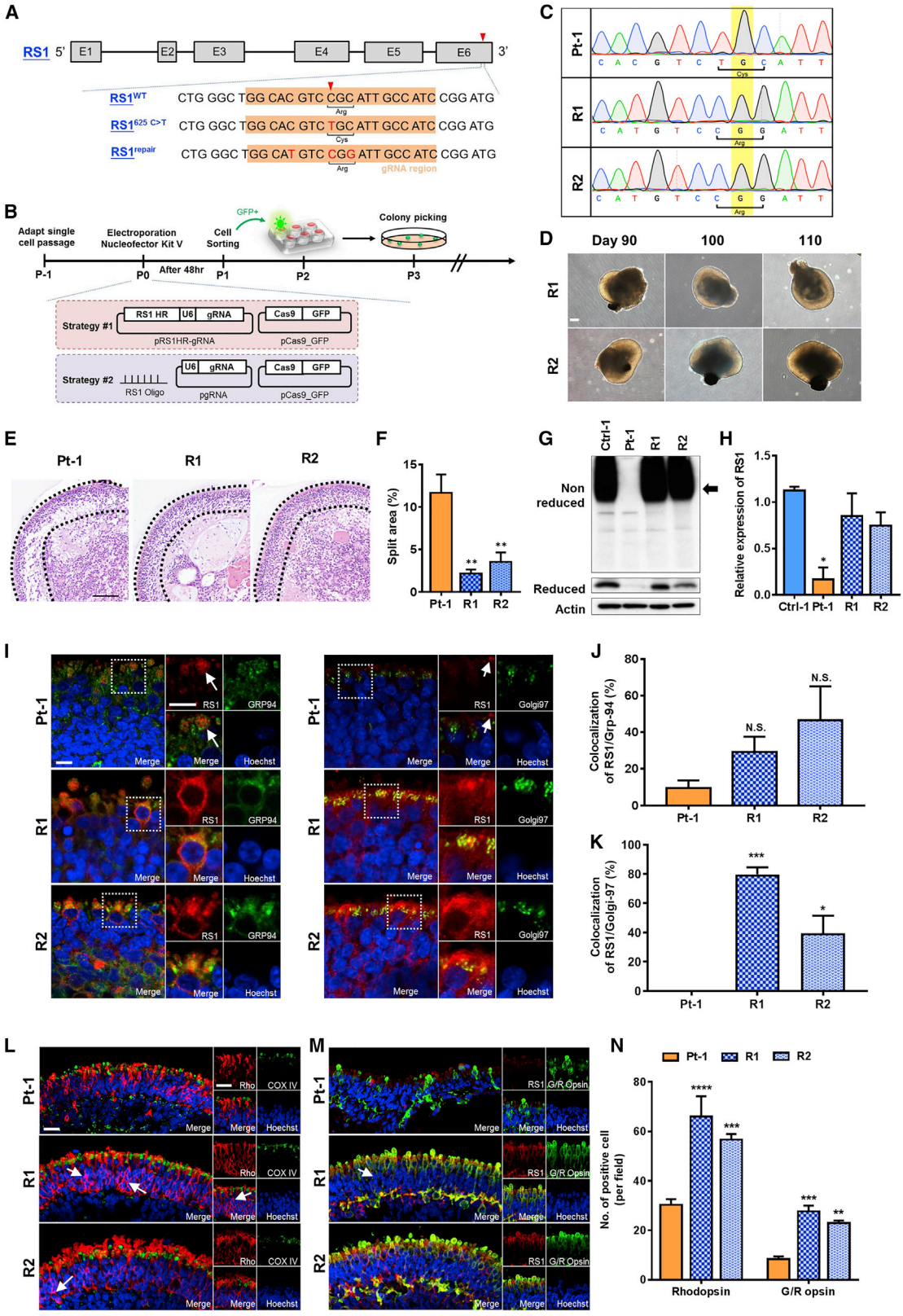

(legend on next page)

Efficient CRISPR/Cas9-Mediated Gene Correction of the C625T Mutation of *RS1* Gene in Patient-Specific hiPSCs

Precise gene editing is a powerful tool for studying and corroborating genotype-phenotype relationships in hiPSC disease modeling, including ophthalmic diseases (Chan et al., 2017). Next, we tested whether the C625T mutation could also be repaired using a recently developed Cas9-directed base-editing approach (Gaudelli et al., 2017). To correct the C625T mutations of *RS1* gene in hiPSCs of patient 1 (Pt-1-hiPSCs) using CRISPR/Cas9 gene editing (Table S2), we designed a guide RNA (gRNA) target sequence and a homologous repair template for converting the mutant Cys codon to an Arg codon, thereby restoring a wild-type *RS1* amino acid sequence (HDR^{Repair}) (Figure 4A). The correction template included two synonymous single-nucleotide changes, at the positions 621 and 627 of *RS1* (Figure 4A), to prevent Cas9 from cutting the template or repaired DNA and to facilitate PCR screening. Moreover, we employed two strategies for the correction of C625T mutation: (1) co-transfection of pCas9_GFP with a plasmid that included both a 950-bp *RS1* repair template and the gRNA expression cassette (pRS1HR-gRNA), and (2) co-transfection of pCas9_GFP, a gRNA expression plasmid, and a 190-nt single-stranded *RS1* repair oligonucleotide (Figure 4B). Both approaches resulted in very high repair efficiencies, with over 50% (plasmid homology template) and 20% (oligo homology template) of the transfected cells having undergone precise repair as determined by droplet digital PCR and confirmed by subcloning and Sanger sequencing. We selected two successfully corrected clones from strategy 1 (R1) and strategy 2 (R2) (Figure 4C). Neither clone showed any off-target mutations at the top-5 most likely gRNA off-target sites (Figure S5). However, many uncorrected clones contained indels. We therefore also evaluated RS1 repair by base editing, which has several advantages over conventional CRISPR/Cas9-induced double-strand break/homology-directed repair, particularly that it does not introduce potentially deleterious indels and that it works much better in post-mitotic cells, including sensory cells (Yeh et al., 2018). When we transfected *RS1* mutant hiPSCs with expression plasmids for GFP, the base editor ABE7.10 (Gaudelli et al., 2017), and a synthetic gRNA, we again achieved a very high repair efficiency (>50%). As expected, despite this high on-target repair efficiency, we did not observe any proximal indels in the base-editing target region of the *RS1* locus (Figure S6). Collectively, we demonstrated efficient and precise on-target CRISPR/Cas9-mediated gene correction of the C625T mutation of the *RS1* gene in patient-specific hiPSCs.

CRISPR/Cas9-Mediated Correction of *RS1* Gene Restores Pathological Phenotype, RS1 Protein Secretion, and the Adhesion Abilities of Retinal Outer Segment in XLRS-iPSC-Derived Retinal Organoids

Following the establishment of *RS1* gene-repaired iPSCs, we differentiated the two repaired hiPSC clones (R1 and

Figure 4. Design of the CRISPR/Cas9-Mediated Gene Correction of *RS1* C625T Mutant hiPSCs

(A) Schematic showing the segment of the *RS1* genome sequence of wild-type (WT), C625T, and C625T corrected (HDR^{repair}) region. The red arrowhead indicates the mutation site of $RS1^{c.625C>T}$; gRNA target region is highlighted.

(B) Diagram of the $RS1^{c.625C>T}$ gene-correction strategy. HR, homologous repair region; U6, gRNA promoter.

(C) Sanger sequencing of *RS1* gene. The yellow bar indicates the location of correction of $RS1^{c.625C>T}$.

(D) Bright-field images of RCs at days 90, 100, and 110 of retinal differentiation in CRISPR/Cas9-repaired clones, R1 and R2. Scale bar, 200 μm.

(E and F) H&E staining of the 150-day control, C625T, R1-RCs, and R2-RCs (E). The areas within the two dotted lines were quantified as the percentage of the splitting layer. Scale bar, 100 μm. (F) Quantification of splitting-layer area in 150-day RCs. The percentage of splitting layer was calculated by the ratio of white (cell-free) area and the total area between ONL and INL of each RC (n = 5 images from 3 independent experiments).

(G and H) Western blotting of RS1 protein expression in 150-day RCs under reducing or non-reducing conditions (G). The arrow indicates the RS1 migrated as ~180-kDa complex in non-reducing condition. Actin was used as internal control. Quantification of RS1 protein expression in 150-day RCs under reducing condition (H). The expression level was normalized to actin (n = 3 from 3 independent experiments).

(I–K) Immunofluorescence staining of RS1 with GRP94 and Golgi97 in 150-day RCs of C625T, R1, and R2 (I). The right panel is a higher-magnification image of the left panel marked with a dotted box. The arrows indicate the prominent mutant RS1-positive signal in C625T-RCs. Scale bar, 10 μm. Quantification of RS1 protein co-localization with GRP94 (J) or Golgi97 (K) (n = 4 images from 3 independent experiments).

(L–N) Immunofluorescence staining of rhodopsin, COX VI (L), G/R opsin, and RS1 (M) in 150-day RCs of C625T, R1, and R2. The arrows indicate normal rod cell morphology. Scale bar, 20 μm. (N) Quantification of cell density of rhodopsin and G/R opsin in 150-day RCs (n = 3 images from 3 independent experiments).

Error bars represent SEM. One-way ANOVA was used for statistical analysis (*$p < 0.05$; **$p < 0.01$; ***$p < 0.001$; ****$p < 0.0001$; N.S., not significant). See also Figures S5 and S6.

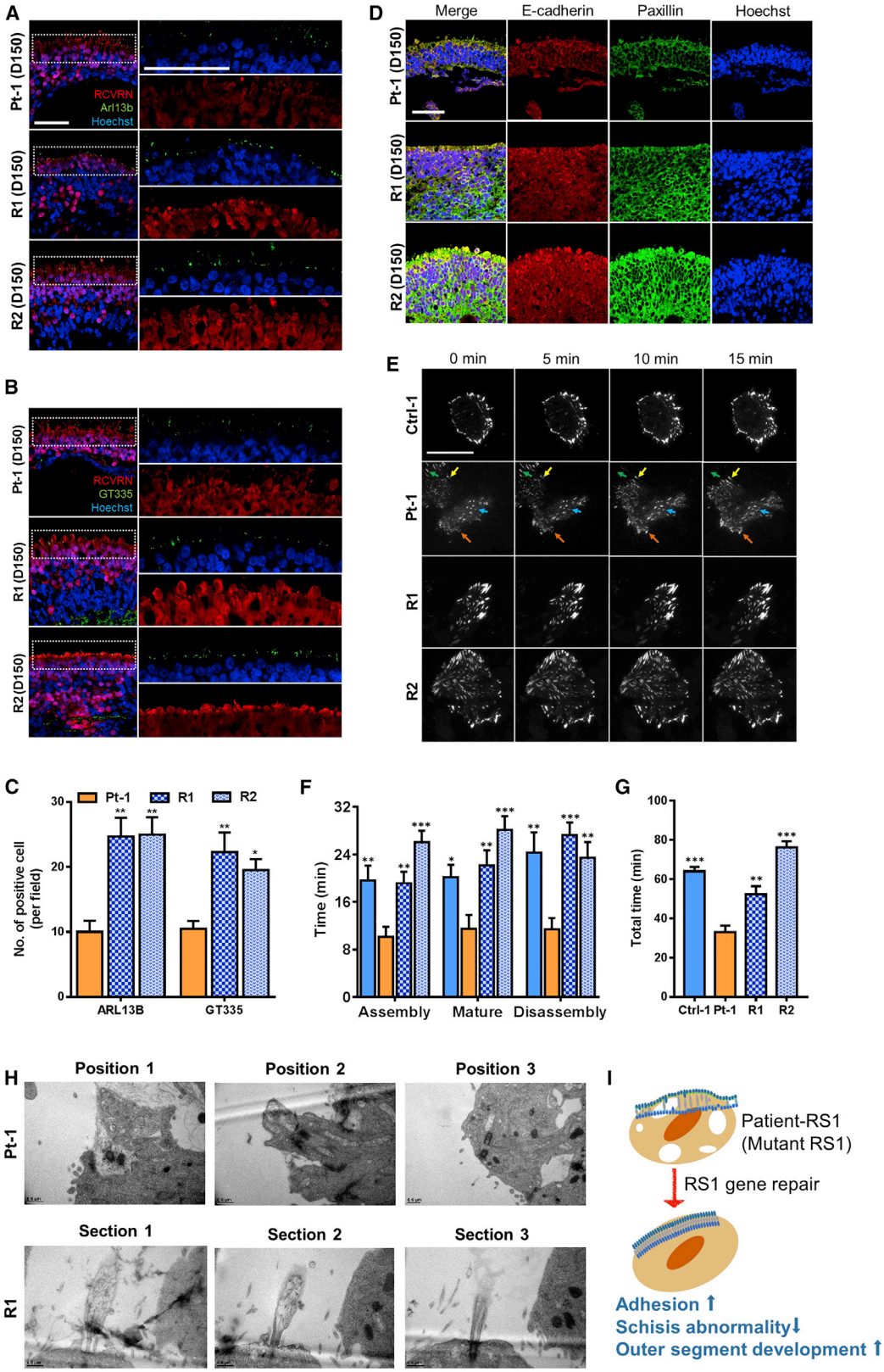

(legend on next page)

R2) into 3D retinal organoids. The repaired clones lacked the disease-specific overt schisis phenotype seen in mutant RCs during differentiation (Figure 4D) and day 150 (Figures 4E and 4F). To investigate whether corrected RS1 regained its ability to form the expected octameric complex and undergo normal intracellular processing in the RCs, we first separated the cell lysate of RCs derived from control, patient-1, and two corrected iPSC clones. RCs from both repaired hiPSC clones were able to produce the 180-kDa RS1 homo-octamer (Figures 4G and 4H). Co-staining of RS1 with GRP94 or Golgi97 revealed enhanced co-localization of RS1 with the ER and Golgi apparatus in 150-day repaired RCs (R1 and R2) compared with unrepaired patient RCs (Figures 4I–4K). These data indicated that repair of the mutated *RS1* gene restored proper intracellular transit, octamerization, and secretion of RS1.

Since patient-derived RCs gave rise to abnormal outer-segment and photoreceptor cells (Figure 2), we next examined these features in repaired RCs. Staining of rhodopsin and G/R opsin revealed an increase in the number of photoreceptor cells and normal outer-segment structure at day 150 in repaired RCs; conversely, the patient RCs contained fewer photoreceptor cells and abnormal outer-segment structures (Figures 4L–4N). Whole-mount staining of 210-day RCs also showed that repaired, but not unrepaired patient RCs contained rhodopsin or G/R opsin-expressing photoreceptor cells in the region of outer segments, as well as blue-opsin-positive cells of normal shape (Figure S3D).

Next, we checked whether connecting cilia and paxillin dynamics were also recovered in repaired RCs. Immunostaining of dissociated 150-day repaired RCs with connecting cilia markers showed that the cilia signals were increased in repaired RCs (Figures 5A–5C) and staining for E-cadherin and paxillin demonstrated a thicker, better organized, and more intact retinal tissue structure as well (Figure 5D). Furthermore, paxillin dynamics were stabilized in dissociated retinal cells from control RCs and repaired RCs compared with C625T-mutant RCs (Figures 5E–5G; Videos S3 and S4). Furthermore, consistent with the recovery of mature photoreceptor cells and ciliary markers as observed by immunofluorescence, TEM analysis revealed that proper outer segments and sensory cilia formed in repaired RCs (Figure 5H). Taken together, CRISPR-mediated *RS1* gene correction resulted in a normalization of the schisis phenotype, increased cilia marker expression, and stabilized paxillin dynamics and recovery of outer-segment structure formation, as well as RS1 secretion (Figure 5I).

CRISPR/Cas9-Directed *RS1* Point Mutation in Control iPSCs Leads to Schisis Phenotype in Differentiated Retinal Organoids

To further ensure that the retinoschisis phenotypes are indeed caused by *RS1* mutation, we used CRISPR/Cas9 gene editing to generate two *RS1* mutated clones (RS1-M1 and RS1-M2) from a healthy donor hiPSC line (Table S2). We designed a single gRNA target sequence and a homologous template for converting the wild-type Arg codon in Ctrl-1 hiPSCs to a Cys codon, thereby creating a mutated *RS1* amino acid sequence (RS1-M1 and RS1-M2; Figures 6A and 6B). At 120 days of organoid differentiation, the CRISPR-induced *RS1* C625T mutation led to large schisis area in RCs in comparison with the control RCs (Figures 6C and 6D). Consistent with previous data, RCs generated from RS1-M1- and RS1-M2-hiPSCs exhibited decreased co-localization of RS1 with GRP94 and Golgi97 (Figures 6E–6G) accompanied by reduced RS1 expression (Figure 6E). Moreover, immunostaining of the photoreceptor markers showed a reduced number of rhodopsin- and G/R opsin-expressing cells (Figures 6H–6J). As expected, the ability of the CRISPR-directed C625T-mutant RS1 protein to form homo-octamer complexes was lost (Figure 6K). In summary, by generating isogenic sets of *RS1* mutant from wild-type control hiPSCs, we were able to confirm strict genotype-phenotype relationships of XLRS. These data also suggest that

Figure 5. Regaining Cilia Formation and Cellular Adhesion in CRISPR/Cas9-Corrected Retinal Organoids

(A–D) Immunofluorescence staining of ARL13B (A) and tubulin GT335 (B) in 150-day RCs. A higher-magnification image in the right panel is the left panel marked with a dotted box. Scale bar, 50 μm. (C) Quantification of cilium density of immunofluorescence in 150-day RCs from higher-magnification images (n = 3 images from 3 independent experiments). (D) Immunofluorescence staining of E-cadherin and paxillin in 150-day RCs. Scale bar, 50 μm.

(E) TIRFM images showing focal adhesion dynamics in photoreceptor cells transfected with mApple-paxillin. The arrows indicate the paxillin dynamics in C625T mutant photoreceptor cells. Scale bar, 40 μm.

(F–H) Quantification of focal adhesion dynamics by measuring assembly, mature state, disassembly (F), and total duration time lapse (G) of mApple-paxillin expression (n = 8 of C625T-RCs, 12 of R1-RCs, and 12 of R2-RCs from 3 independent experiments). (H) Transmission electron micrographs of 210-day RCs from Pt-1 (top) and R1 (bottom) iPSCs. The photos of Pt-1 were taken from three different positions of RCs and the photos of R1 were taken from three sequential sections to show the structure of centriole and photoreceptor-like structure. Scale bar, 0.5 μm.

(I) Schematic presentation of the effects of RS1 mutation on retinal phenotype. Error bars represent SEM. One-way ANOVA was used for statistical analysis (*$p < 0.05$; **$p < 0.01$; ***$p < 0.001$). See also Videos S3 and S4.

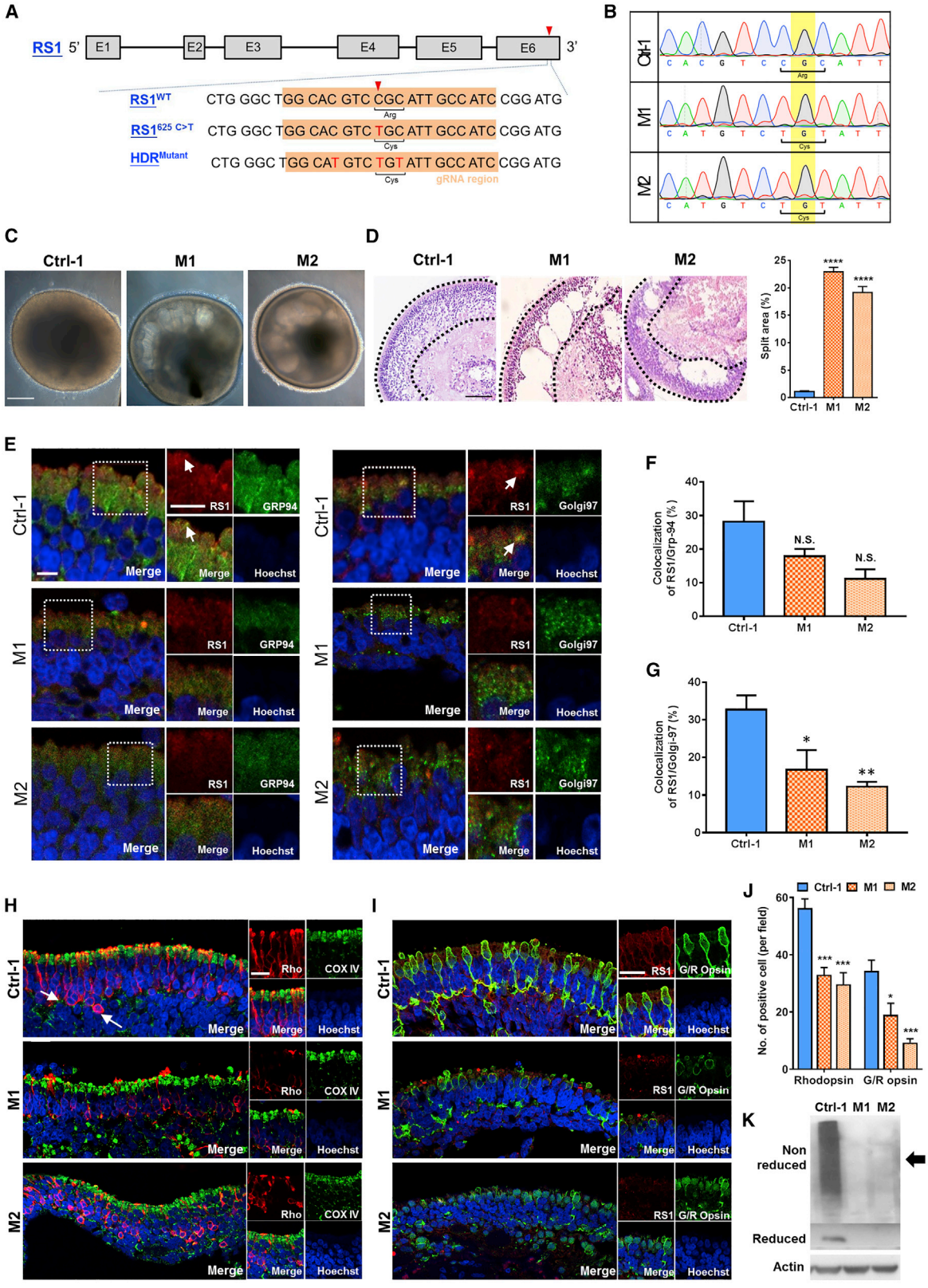

(legend on next page)

CRISPR/Cas9-directed gene editing is a potential platform to generate an *in vitro* study model for diseases caused by defined gene mutation such as XLRS.

RNA Sequencing Reveals Reduced Expression of Two Other Ophthalmic Disease Genes, *IQBT1* and *OPA1*, in *RS1*-Mutant Retinal Organoids

To gain further insights into the molecular defects in XLRS, we performed deep sequencing of the total RNA extracted from control RCs, patient RCs (Pt-1, c.625C>T), R1-RCs, and R2-RCs at various time points (days 0–150). As shown by Pearson correlation analysis, the transcriptomes of control RCs and C625T-RCs considerably diverged along the time course of differentiation, with the difference becoming more pronounced at the later time points (Figure 7A). In contrast, analysis of repaired RCs revealed transcriptomes that were highly similar to those of control RCs and significantly different from those of patient RCs (Figure 7B). Because RS1 is only expressed in the later stage of differentiation, we focused on days 90, 120, and 150 post induction and analyzed the genes whose expression was reduced at least 2-fold in patient RCs (Figure 7C). Among all of these genes, 326 genes were overexpressed in normal RCs at all of these stages (Table S4), emphasizing their importance (Figure 7D, left). According to gene set enrichment analysis (GSEA) annotation, 9 out of these 326 genes were implicated in eye development (Figure 7D, right). Notably, among these nine genes the expression of *RS1*, *IQCB1*, and *OPA1* was rescued in CRISPR-repaired RCs (Figure 7E). The relative loss of expression became even more prominent in later stages of retinal differentiation (Figure 7F). Notably, *IQCB1* mutations are associated with Leber congenital amaurosis, a ciliopathy that affects the retina, and *IQCB1* mutant retinas fail to produce mature photoreceptor cells with outer segments (Ronquillo et al., 2016), reminiscent of what we observed in this study with *RS1* mutant RCs. *OPA1*, on the other hand, is a mitochondrial fusion protein that has been linked to autosomal dominant optic atrophy, a degenerative condition that affects retinal ganglion cells (Ronquillo et al., 2016; Wang et al., 2006). Thus, the results of our transcriptomics analysis reflect the progressive nature of the disease phenotypes observed in *RS1*-mutant RCs, mirror the observed ciliary phenotype, and reveal potential links of XLRS to other hereditary retinopathies.

DISCUSSION

XLRS is an early-onset congenital macular degeneration associated with the *RS1* gene (Molday et al., 2012). RS1 protein is necessary for a complex interplay between distinct cell types and layers in laminated retinal tissue, as it is present in the inner segments of rod and cone photoreceptors, the outer plexiform layer (OPL), and the INL (Molday et al., 2001). Conventional methods of differentiating human embryonic stem cells or hiPSCs into retinal cell lineages use a two-dimensional culture system, and the resultant retinal cells lack tissue architectural features typical for *in vivo* retina. However, generation of properly laminated retinal tissues (Figure 1C) (Zhong et al., 2014) is uniquely suitable for addressing such complex interactions and more similar to the development of the human retina *in vivo* (Marangoni et al., 2016). In our study, we used retinal organoids derived from XLRS-hiPSCs, thus creating a human *in vitro* model of XLRS. *RS1* mutant RCs mirror the retinal schisis phenotype seen in patients, exhibit RS1 protein production/maturation defects, and produce fewer and mostly

Figure 6. Characterization of RCs Derived from CRISPR/Cas9-Inserted C625T Mutation

(A) Schematic showing the segment of the *RS1* genome sequence of wild-type (WT), C625T, and inserted mutation (HDR^{mutant}) region. The red arrowhead indicates the mutation site of $RS1^{c.625C>T}$; gRNA target region is highlighted.

(B) Sanger sequencing of *RS1* gene. The yellow bar indicates the location of correction/insertion of $RS1^{c.625C>T}$.

(C) Bright-field images of 150-day RCs differentiated from Ctrl-1, M1, and M2 iPSC clones. Scale bar, 200 μm.

(D) H&E staining of the 150-day control, M1-RCs, and M2-RCs. The areas within the two dotted lines were quantified as the percentage of splitting layer. The percentage of splitting layer was calculated by the ratio of the white (cell-free) area and the total area between outer nuclear layer and inner nuclear layer of each RC. Scale bar, 100 μm. The quantification of splitting-layer area in 150-day RCs is shown in the right panel (n = 5 images from 3 independent experiments).

(E) Immunofluorescence staining of RS1 with GRP94 and Golgi97 in 150-day RCs of Ctrl-1, M1, and M2. The right panel is a higher-magnification image of the left panel marked with a dotted box. Scale bar, 10 μm.

(F and G) Quantification of RS1 protein co-localization with GRP94 (F) or Golgi97 (G) (n = 4 images from 3 independent experiments).

(H and I) Immunofluorescence staining of rhodopsin, COX VI (H), G/R opsin, and RS1 (I) in 150-day Ctrl-1 RCs, M1-RCs, and M2-RCs. The arrows indicate normal rod cell morphology. Scale bar, 20 μm.

(J) Quantification of cell density of rhodopsin and G/R opsin in 150-day RCs (n = 3 images from 3 independent experiments).

(K) Western blotting of RS1 protein expression in 120-day Ctrl-1 RCs, M1-RCs, and M2-RCs under reducing or non-reducing conditions. The arrow indicates the RS1 migrated as ~180-kDa complex in non-reducing condition. Actin was used as internal control.

Error bars represented SEM. One-way ANOVA was used for statistical analysis (*$p < 0.05$; **$p < 0.01$; ***$p < 0.001$; ****$p < 0.0001$; N.S., not significant).

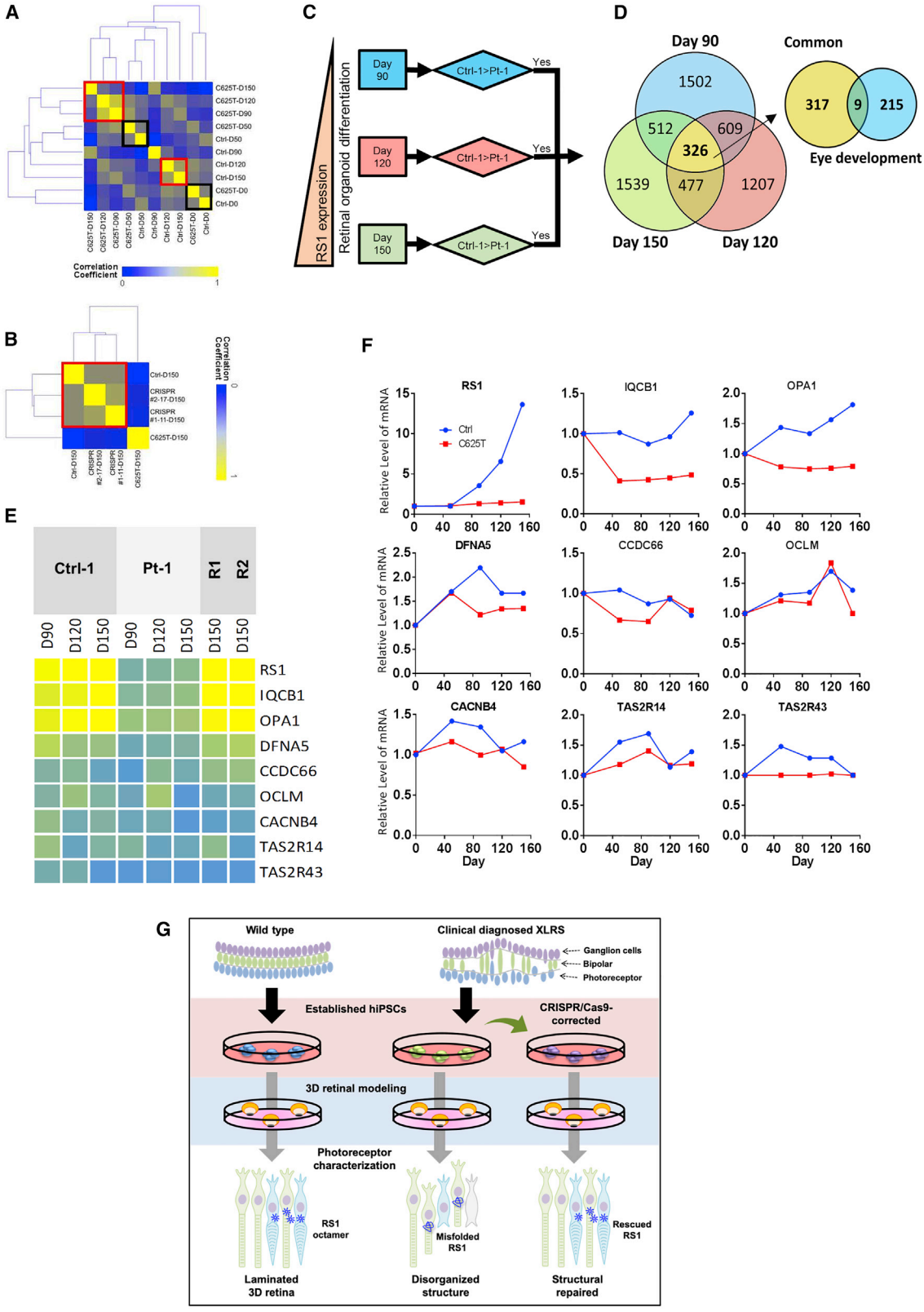

(legend on next page)

abnormal photoreceptors with fewer connecting cilia. Furthermore, dissociated *RS1*-mutant RC cells showed altered paxillin dynamics (Table S3).

By modeling human retinal development *in vitro*, we showed that *RS1* is critical for the structural integrity of the retinal layers in 3D organoids (Figures 2A–2C). In the *Rs1*-knockout mice, mutant retinas were characterized by delayed rod cell maturation and a higher threshold for light-driven transducing translocation (Ziccardi et al., 2012, 2014). However, this study shed little light on the effects on cone cells (the cells most critical for resolving colors and fine details), since cone cells are much less frequent near the center of murine versus human foveas (Volland et al., 2015), the area most critical for high visual acuity. Our results highlight the utility of the hiPSC-RC system for a more precise modeling of human retinopathies, and revealed that pathological *RS1* mutations result in defective rod and cone cells.

Notably, we generated multiple sets of isogenic hiPSCs to confirm specificity of the genotype-phenotype relationships. Precise gene repair of the *RS1* locus generated isogenic clones in which all of the molecular and structural deficiencies observed in patient-derived RCs were reversed (Figures 4 and 5A–5C) and normal paxillin dynamics were restored (Figures 5E–5G). We also generated *RS1* C625T mutation clones from control-donor-derived clones through CRISPR/Cas9 gene editing; this panel of isogenic control and CRISPR/Cas9-directed *RS1* mutation clones possess an identical genetic background except for *RS1*, and thus served as an ideal model to study the pathogenic effect of *RS1* mutation during retinal development (Figure 6). These isogenic CRISPR/Cas9-repaired and CRISPR/Cas9-directed *RS1* mutant RCs are particularly valuable in revealing the phenotype differences that are specific to the *RS1* mutation.

In addition to the previous view that RS1 plays a role in cellular adhesion, mediating cell communication, and providing structural support for the retinal layers (Piermarocchi et al., 2017; Wu et al., 2005), our transcriptome analysis revealed significant changes in gene expression between patient-derived and control RCs that become more pronounced at the later stages of development. This implies that RS1 is essential for normal retinal development at the systemic level, possibly secondary to the structural and cell-communication defects. Importantly, the transcriptomes of CRISPR/Cas9-repaired hiPSCs were more similar to those of controls. In an attempt to identify important genes whose expression is abrogated by *RS1* mutation and rescued by CRISPR/Cas9 repair, we identified *IQCB1* and *OPA1*, encoding Nephrocystin-5 and mitochondrial dynamin like guanosine triphosphatase, respectively. The *IQCB1* gene product is localized to the transition zone of connecting cilia. Consistent with the ciliary and outer-segment defects that we observed in *RS1*-mutated RCs, *IQCB1* is critical for the formation of outer segments and has been linked to another retinopathy called Leber congenital amaurosis, a hereditary ciliopathy (Ronquillo et al., 2016). *OPA1*, expressed primarily in the inner segment and OPLs (Kam and Jeffery, 2015), is a nuclear mitochondrial fusion gene associated with optic atrophy type 1 (Wang et al., 2006). The loss of OPA1 expression thus may be related the impaired communication between sensory cells and other neuronal cells in the retina and the atrophy of the optic nerve that is seen in many XLRS patients (Genead et al., 2009). To summarize, our RNA-sequencing data provide new molecular links of XLRS to other retinopathies with overlapping clinical phenotypes. Furthermore, the numerous and progressive gene-expression changes point to additional direct or indirect (secondary to structural, adhesive, and ciliary defects) roles of RS1 in multiple retinal processes and cell types.

Collectively, we showed that the XLRS patient-specific hiPSC-derived 3D retinal organoids can serve as a powerful model system for investigating the pathophysiological mechanism of this retinopathy. Our data revealed for the first time the causative role of *RS1* mutations in a human *in vitro* system that allows detailed investigations of prenatal retinal development and of the molecular and cellular mechanisms that underlie XLRS. Our study identifies potential new targets for therapeutic intervention, such as Paxillin and FIS1 (an antagonist of OPA1 [Lee et al., 2007]) and suggests that development of the pathological phenotypes may be preventable if efficient *in vivo* repair

Figure 7. RNA Sequencing Reveals the *RS1*-Associated Changes of Gene-Expression Landscape

(A) Pearson correlation analysis of gene-expression profiles in Ctrl-1 RCs and Pt-1 RCs at different time points of differentiation.

(B) Pearson correlation matrix showing similarity between gene-expression profiles of 150-day Ctrl-1-, Pt-1-, R1-, and R2-RCs.

(C) The pipeline of selecting differentially expressed genes at three post-induction time points of retinal differentiation.

(D) Left: Venn diagram demonstrating the numbers of common and unique differentially expressed genes between different stages of differentiation. Right: Venn diagram demonstrating the number of common genes between 326 genes differentially expressed at all stages of differentiation and 215 genes of GSEA annotation "Eye development."

(E) Gene-expression matrix of the nine genes identified in (D).

(F) Time-course expression levels of the nine genes differentially expressed in control RCs and C625T-RCs are shown in the charts.

(G) Schematic of disease modeling from human 3D retinal organoid of XLRS.

(such as by base editing) at the earliest time can be achieved. Our *in vitro* model system may prove useful to identify and validate targets for intervention as well as to develop and optimize therapeutic approaches, including *in vivo* gene therapy.

EXPERIMENTAL PROCEDURES

Retinal Organoid Differentiation from Human iPSC Lines

The method of differentiation into retinal organoids followed previous methods with slight modifications (Ohlemacher et al., 2015; Wahlin et al., 2017; Zhong et al., 2014). Details of the differentiation procedure are presented in Supplemental Experimental Procedures.

CRISPR/Homology-Directed Repair *RS1* Gene-Editing Agents

The pCas9-GFP plasmid was used as previously described (Burnight et al., 2017). The guide RNA sequence (targeting sequence underlined) was GGC ACG TCT GCA TTG CCA TCG TTT TAG AGC TAG AAA TAG CAA GTT AAA ATA AGG CTA GTC CGT TAT CAA CTT GAA AAA GTG GCA CCG AGT CGG TGC. The 190-b RS1 oligo repair-template sequence was GTC TTC TAT GGC AAC TCG GAC CGC ACC TCC ACG GTT CAG AAC CTG CTG CGG CCC CCC ATC ATC TCC CGC TTC ATC CGC CTC ATC CCG CTG GGC TGG CAT GTC CGG ATT GCC ATC CGG ATG GAG CTG CTG GAG TGC GTC AGC AAG TGT GCC TGA TGC CTG CCT CAG CTC GGC GCC TGC CAG GGG GTG ACT G. The 950-bp RS1 genomic sequence plasmid insert for homology-directed repair of the C625T mutation contained the repair oligo sequence in its center. Conversely, to introduce the C625T (Arg209Cys) mutation in normal male hiPSC, the HDR template sequence included the C to T point mutation at the *RS1* nucleotide position 625, as well as two silent mutations, C to T at position 621 and C to T at position 627, to facilitate genotyping and reduce cutting of the edited locus or template (Figure 4A).

Other material and methods are detailed in Supplemental Experimental Procedures.

SUPPLEMENTAL INFORMATION

Supplemental Information can be found online at https://doi.org/10.1016/j.stemcr.2019.09.010.

AUTHOR CONTRIBUTIONS

K.-C.H. and M.-L.W. contributed equally. S.-J.C., J.-C.K., W.-J.W., P.N.N.N. also contributed equally. Conceptualization: K.-C.H., M.-L.W., T.M.S., and S.-H.C. hiPSC establishment, differentiation and data analysis: K.-C.H., M.-L.W., P.N.N.N., and T.-C.Y. RNA-seq analysis: Y.C., P.-H.T., A.A.Y., C.-C.C., and M.-L.W. TEM and cilia analysis: W.-J.W. and W.-N.J. and K.-C.H. Cellular adhesion and cytoskeleton analysis: J.-C.K. and K.-C.H. Resources: S.-J.C., C.-H.P., and S.-H.C. RS1 genotyping: J.-F.L. Genome editing, base editing, hiPSC culture, and QC experiments: A.A.T., M.S., and T.M.S. Data interpretation and discussion: K.J.W., S.-J.C., K.-C.H., M.-L.W., T.M.S., and S.-H.C. Writing: K.-C.H., M.-L.W., K.J.W., T.M.S., and S.-H.C. Supervision: T.M.S., and S.-H.C.

ACKNOWLEDGMENTS

We thank Li-Ju Lin BS for excellent technical assistance. This study was funded by the Ministry of Science and Technology (MOST) of Taiwna and Academic Sinica of Taiwan (107-2633-B-009-003), Taipei Veterans General Hospital of Taiwan (V107E-002-2, V108E-006-4, and V108D46-004-MY2-1), the Department of Health Cancer Center Research of Excellence of Taiwan (MOHW106-TDU-B-211-144003), the Excellent Clinical Trail Center of Taiwan (107-TDU-B-211-123001/MOHW108-TDU-B-211-133001), NRPB Human iPSC Alliance-Core Service of Taiwan (MOST 105-2325-B-010-005), VGH, TSGH, NDMC, AS Joint Research Program of Taiwan (VTA105-V1-5-1/107-V1-5-1/V108-V1-5-1), VGH, NTUH Joint Research Program of Taiwan (VN106-02/VN107-16/VN108-2), NHRI (NHRI-EX107-10621BI), and the "Center for Intelligent Drug Systems and Smart Bio-devices (IDS2B)" of NCTU, "Cancer Progression Research Center" of NYMU from The Featured Areas Research Center Program within the framework of the Higher Education Sprout Project by the Ministry of Education (MOE) in Taiwan.

Received: June 12, 2018
Revised: September 25, 2019
Accepted: September 26, 2019
Published: October 24, 2019

REFERENCES

Adams, N.A., Awadein, A., and Toma, H.S. (2007). The retinal ciliopathies. Ophthalmic Genet. *28*, 113–125.

Burnight, E.R., Gupta, M., Wiley, L.A., Anfinson, K.R., Tran, A., Triboulet, R., Hoffmann, J.M., Klaahsen, D.L., Andorf, J.L., Jiao, C., et al. (2017). Using CRISPR-Cas9 to generate gene-corrected autologous iPSCs for the treatment of inherited retinal degeneration. Mol. Ther. *25*, 1999–2013.

Chan, L., Mahajan, V.B., and Tsang, S.H. (2017). Genome surgery and gene therapy in retinal disorders. Yale J. Biol. Med. *90*, 523–532.

Chou, S.J., Yu, W.C., Chang, Y.L., Chen, W.Y., Chang, W.C., Chien, Y., Yen, J.C., Liu, Y.Y., Chen, S.J., Wang, C.Y., et al. (2017). Energy utilization of induced pluripotent stem cell-derived cardiomyocyte in Fabry disease. Int. J. Cardiol. *232*, 255–263.

De Robertis, E. (1956). Morphogenesis of the retinal rods; an electron microscope study. J. Biophys. Biochem. Cytol. *2*, 209–218.

Deng, W.L., Gao, M.L., Lei, X.L., Lv, J.N., Zhao, H., He, K.W., Xia, X.X., Li, L.Y., Chen, Y.C., Li, Y.P., et al. (2018). Gene correction reverses ciliopathy and photoreceptor loss in iPSC-derived retinal organoids from retinitis pigmentosa patients. Stem Cell Reports *10*, 1267–1281.

Garanto, A., van Beersum, S.E., Peters, T.A., Roepman, R., Cremers, F.P., and Collin, R.W. (2013). Unexpected CEP290 mRNA splicing in a humanized knock-in mouse model for Leber congenital amaurosis. PLoS One *8*, e79369.

Gaudelli, N.M., Komor, A.C., Rees, H.A., Packer, M.S., Badran, A.H., Bryson, D.I., and Liu, D.R. (2017). Programmable base editing of A*T to G*C in genomic DNA without DNA cleavage. Nature *551*, 464–471.

Genead, M.A., Pasadhika, S., and Fishman, G.A. (2009). Retinal nerve fibre layer thickness analysis in X-linked retinoschisis using Fourier-domain OCT. Eye (Lond.) *23*, 1019–1027.

George, N.D., Yates, J.R., and Moore, A.T. (1995). X linked retinoschisis. Br. J. Ophthalmol. *79*, 697–702.

Kam, J.H., and Jeffery, G. (2015). To unite or divide: mitochondrial dynamics in the murine outer retina that preceded age related photoreceptor loss. Oncotarget *6*, 26690–26701.

Lee, S., Jeong, S.Y., Lim, W.C., Kim, S., Park, Y.Y., Sun, X., Youle, R.J., and Cho, H. (2007). Mitochondrial fission and fusion mediators, hFis1 and OPA1, modulate cellular senescence. J. Biol. Chem. *282*, 22977–22983.

Liang, M., Cai, T., Tian, J., Qu, W., and Xie, Z.J. (2006). Functional characterization of Src-interacting Na/K-ATPase using RNA interference assay. J. Biol. Chem. *281*, 19709–19719.

Liu, X., Wu, T.H., Stowe, S., Matsushita, A., Arikawa, K., Naash, M.I., and Williams, D.S. (1997). Defective phototransductive disk membrane morphogenesis in transgenic mice expressing opsin with a mutated N-terminal domain. J. Cell Sci. *110* (Pt 20), 2589–2597.

Marangoni, D., Bush, R.A., Zeng, Y., Wei, L.L., Ziccardi, L., Vijayasarathy, C., Bartoe, J.T., Palyada, K., Santos, M., Hiriyanna, S., et al. (2016). Ocular and systemic safety of a recombinant AAV8 vector for X-linked retinoschisis gene therapy: GLP studies in rabbits and Rs1-KO mice. Mol. Ther. Methods Clin. Dev. *5*, 16011.

Meyer, J.S., Howden, S.E., Wallace, K.A., Verhoeven, A.D., Wright, L.S., Capowski, E.E., Pinilla, I., Martin, J.M., Tian, S., Stewart, R., et al. (2011). Optic vesicle-like structures derived from human pluripotent stem cells facilitate a customized approach to retinal disease treatment. Stem Cells *29*, 1206–1218.

Molday, L.L., Hicks, D., Sauer, C.G., Weber, B.H., and Molday, R.S. (2001). Expression of X-linked retinoschisis protein RS1 in photoreceptor and bipolar cells. Invest. Ophthalmol. Vis. Sci. *42*, 816–825.

Molday, L.L., Wu, W.W., and Molday, R.S. (2007). Retinoschisin (RS1), the protein encoded by the X-linked retinoschisis gene, is anchored to the surface of retinal photoreceptor and bipolar cells through its interactions with a Na/K ATPase-SARM1 complex. J. Biol. Chem. *282*, 32792–32801.

Molday, R.S., Kellner, U., and Weber, B.H. (2012). X-linked juvenile retinoschisis: clinical diagnosis, genetic analysis, and molecular mechanisms. Prog. Retin. Eye Res. *31*, 195–212.

Mustafi, D., Engel, A.H., and Palczewski, K. (2009). Structure of cone photoreceptors. Prog. Retin. Eye Res. *28*, 289–302.

Ohlemacher, S.K., Iglesias, C.L., Sridhar, A., Gamm, D.M., and Meyer, J.S. (2015). Generation of highly enriched populations of optic vesicle-like retinal cells from human pluripotent stem cells. Curr. Protoc. Stem Cell Biol. *32*, 1H 8 1–20.

Ohlemacher, S.K., Sridhar, A., Xiao, Y., Hochstetler, A.E., Sarfarazi, M., Cummins, T.R., and Meyer, J.S. (2016). Stepwise differentiation of retinal ganglion cells from human pluripotent stem cells enables analysis of glaucomatous neurodegeneration. Stem Cells *34*, 1553–1562.

Okita, K., Yamakawa, T., Matsumura, Y., Sato, Y., Amano, N., Watanabe, A., Goshima, N., and Yamanaka, S. (2013). An efficient nonviral method to generate integration-free human-induced pluripotent stem cells from cord blood and peripheral blood cells. Stem Cells *31*, 458–466.

Parfitt, D.A., Lane, A., Ramsden, C.M., Carr, A.J., Munro, P.M., Jovanovic, K., Schwarz, N., Kanuga, N., Muthiah, M.N., Hull, S., et al. (2016). Identification and correction of mechanisms underlying inherited blindness in human iPSC-derived optic cups. Cell Stem Cell *18*, 769–781.

Peirson, S.N., Brown, L.A., Pothecary, C.A., Benson, L.A., and Fisk, A.S. (2018). Light and the laboratory mouse. J. Neurosci. Methods *300*, 26–36.

Peng, C.-H., Huang, K.-C., Lu, H.-E., Syu, S.-H., Yarmishyn, A.A., Lu, J.-F., Buddhakosai, W., Lin, T.-C., Hsu, C.-C., Hwang, D.-K., et al. (2018). Generation of induced pluripotent stem cells from a patient with X-linked juvenile retinoschisis. Stem Cell Res. *29*, 152–156.

Piermarocchi, S., Miotto, S., Colavito, D., Del Giudice, E., Leon, A., Maritan, V., Piermarocchi, R., and Tormene, A.P. (2017). Long-term rearrangement of retinal structures in a novel mutation of X-linked retinoschisis. Biomed. Rep. *7*, 241–246.

Plossl, K., Royer, M., Bernklau, S., Tavraz, N.N., Friedrich, T., Wild, J., Weber, B.H.F., and Friedrich, U. (2017). Retinoschisin is linked to retinal Na/K-ATPase signaling and localization. Mol. Biol. Cell *28*, 2178–2189.

Reid, S.N., Yamashita, C., and Farber, D.B. (2003). Retinoschisin, a photoreceptor-secreted protein, and its interaction with bipolar and muller cells. J. Neurosci. *23*, 6030–6040.

Richardson, A., Malik, R.K., Hildebrand, J.D., and Parsons, J.T. (1997). Inhibition of cell spreading by expression of the C-terminal domain of focal adhesion kinase (FAK) is rescued by coexpression of Src or catalytically inactive FAK: a role for paxillin tyrosine phosphorylation. Mol. Cell Biol. *17*, 6906–6914.

Ronquillo, C.C., Hanke-Gogokhia, C., Revelo, M.P., Frederick, J.M., Jiang, L., and Baehr, W. (2016). Ciliopathy-associated IQCB1/NPHP5 protein is required for mouse photoreceptor outer segment formation. FASEB J. *30*, 3400–3412.

Sauer, C.G., Gehrig, A., Warneke-Wittstock, R., Marquardt, A., Ewing, C.C., Gibson, A., Lorenz, B., Jurklies, B., and Weber, B.H. (1997). Positional cloning of the gene associated with X-linked juvenile retinoschisis. Nat. Genet. *17*, 164–170.

Singh, R., Shen, W., Kuai, D., Martin, J.M., Guo, X., Smith, M.A., Perez, E.T., Phillips, M.J., Simonett, J.M., Wallace, K.A., et al. (2013). iPS cell modeling of Best disease: insights into the pathophysiology of an inherited macular degeneration. Hum. Mol. Genet. *22*, 593–607.

Takada, Y., Fariss, R.N., Muller, M., Bush, R.A., Rushing, E.J., and Sieving, P.A. (2006). Retinoschisin expression and localization in rodent and human pineal and consequences of mouse RS1 gene knockout. Mol. Vis. *12*, 1108–1116.

Tantri, A., Vrabec, T.R., Cu-Unjieng, A., Frost, A., Annesley, W.H., Jr., and Donoso, L.A. (2004). X-linked retinoschisis: a clinical and molecular genetic review. Surv. Ophthalmol. *49*, 214–230.

Volland, S., Esteve-Rudd, J., Hoo, J., Yee, C., and Williams, D.S. (2015). A comparison of some organizational characteristics of the mouse central retina and the human macula. PLoS One *10*, e0125631.

Wahlin, K.J., Maruotti, J.A., Sripathi, S.R., Ball, J., Angueyra, J.M., Kim, C., Grebe, R., Li, W., Jones, B.W., and Zack, D.J. (2017). Photoreceptor outer segment-like structures in long-term 3D retinas from human pluripotent stem cells. Sci. Rep. *7*, 766.

Wang, A.G., Fann, M.J., Yu, H.Y., and Yen, M.Y. (2006). OPA1 expression in the human retina and optic nerve. Exp. Eye Res. *83*, 1171–1178.

Wang, T., Waters, C.T., Rothman, A.M., Jakins, T.J., Romisch, K., and Trump, D. (2002). Intracellular retention of mutant retinoschisin is the pathological mechanism underlying X-linked retinoschisis. Hum. Mol. Genet. *11*, 3097–3105.

Wu, W.W., and Molday, R.S. (2003). Defective discoidin domain structure, subunit assembly, and endoplasmic reticulum processing of retinoschisin are primary mechanisms responsible for X-linked retinoschisis. J. Biol. Chem. *278*, 28139–28146.

Wu, W.W., Wong, J.P., Kast, J., and Molday, R.S. (2005). RS1, a discoidin domain-containing retinal cell adhesion protein associated with X-linked retinoschisis, exists as a novel disulfide-linked octamer. J. Biol. Chem. *280*, 10721–10730.

Xu, L., Overbeek, P.A., and Reneker, L.W. (2002). Systematic analysis of E-, N- and P-cadherin expression in mouse eye development. Exp. Eye Res. *74*, 753–760.

Yeh, W.H., Chiang, H., Rees, H.A., Edge, A.S.B., and Liu, D.R. (2018). In vivo base editing of post-mitotic sensory cells. Nat. Commun. *9*, 2184.

Zaidel-Bar, R., Milo, R., Kam, Z., and Geiger, B. (2007). A paxillin tyrosine phosphorylation switch regulates the assembly and form of cell-matrix adhesions. J. Cell Sci. *120*, 137–148.

Zhong, X., Gutierrez, C., Xue, T., Hampton, C., Vergara, M.N., Cao, L.H., Peters, A., Park, T.S., Zambidis, E.T., Meyer, J.S., et al. (2014). Generation of three-dimensional retinal tissue with functional photoreceptors from human iPSCs. Nat. Commun. *5*, 4047.

Ziccardi, L., Vijayasarathy, C., Bush, R.A., and Sieving, P.A. (2012). Loss of retinoschisin (RS1) cell surface protein in maturing mouse rod photoreceptors elevates the luminance threshold for light-driven translocation of transducin but not arrestin. J. Neurosci. *32*, 13010–13021.

Ziccardi, L., Vijayasarathy, C., Bush, R.A., and Sieving, P.A. (2014). Photoreceptor pathology in the X-linked retinoschisis (XLRS) mouse results in delayed rod maturation and impaired light driven transducin translocation. Adv. Exp. Med. Biol. *801*, 559–566.